Icarus 215 (2011) 682–694

Contents lists available at ScienceDirect

Icarus

journal homepage: www.elsevier.com/locate/icarus

Saturn's F ring grains: Aggregates made of crystalline water ice

Sanaz Vahidinia *, Jeffrey N. Cuzzi, Matt Hedman, Bruce Draine, Roger N. Clark, Ted Roush, Gianrico Filacchione, Philip D. Nicholson, Robert H. Brown, Bonnie Buratti, Christophe Sotin

NASA Post Doctoral Program, Space Science Division, Ames Research Center, Mail Stop 245-3, NASA Moffett Field, CA 94035, USA

ARTICLE INFO

Article history:
Available online 13 July 2011

Keywords:
Planetary rings
Saturn, Rings
Ices, IR spectroscopy
Radiative transfer

ABSTRACT

We present models of the near-infrared (1–5 μm) spectra of Saturn's F ring obtained by Cassini's Visual and Infrared Mapping Spectrometer (VIMS) at ultra-high phase angles (177.4–178.5°). Modeling this spectrum constrains the size distribution, composition, and structure of F ring particles in the 0.1–100 μm size range. These spectra are very different from those obtained at lower phase angles; they lack the familiar 1.5 and 2 μm absorption bands, and the expected 3 μm water ice primary absorption appears as an unusually narrow dip at 2.87 μm. We have modeled these data using multiple approaches. First, we use a simple Mie scattering model to constrain the size distribution and composition of the particles. The Mie model allows us to understand the overall shapes of the spectra in terms of dominance by diffraction at these ultra-high phase angles, and also to demonstrate that the 2.87 μm dip is associated with the Christiansen frequency of water ice (where the real refractive index passes unity). Second, we use a combination of Mie scattering with Effective Medium Theory to probe the effect of porous (but structureless) particles on the overall shape of the spectrum and depth of the 2.87 μm band. Such simple models are not able to capture the shape of this absorption feature well. Finally, we model each particle as an aggregate of discrete monomers, using the Discrete Dipole Approximation (DDA) model, and find a better fit for the depth of the 2.87 μm feature. The DDA models imply a slightly different overall size distribution. We present a simple heuristic model which explains the differences between the Mie and DDA model results. We conclude that the F ring contains aggregate particles with a size distribution that is distinctly narrower than a typical power law, and that the particles are predominantly crystalline water ice.

1. Introduction

Saturn's multi-stranded F ring lies just outside of the main rings. It consists of a narrow inner core, approximately 50 km wide (Murray et al., 2008; Bosh et al., 1997) surrounded by multiple strands with variable positions and structure (Charnoz et al., 2005; Smith et al., 1981, 1982; Murray et al., 1997). Voyager observations led to the discovery of two moons, Prometheus and Pandora, one on either side of the F ring. This configuration led to the belief that these satellites caused and maintained the narrow structure of the F ring. However, a number of arguments have been raised against this idea (Showalter and Burns, 1982; Cuzzi and Burns, 1988; Barbara and Esposito, 2002) and the situation has become even more complicated as the F ring's structure has changed considerably since Voyager (Showalter et al., 2009; Murray et al., 2008).

The F ring lies in a very dynamic and perhaps even chaotic environment (Scargle et al., 1993; Winter et al., 2007) with clumps and strands forming and disappearing on various time scales. The discontinuous core has a 1 km narrow component with an optical depth of 0.1 (see Section 3.3 for definition of optical depth) composed of centimeter-sized particles, which was first seen in radio observations (Lane et al., 1982; Tyler et al., 1983). Despite its possibly chaotic environment, the core appears to maintain a nearly constant eccentricity and uniform precession rate (Bosh et al., 2002; Nicholson et al., 2000). This has led to the belief that most of the mass of the F ring is concentrated in this narrow component, which is embedded in a haze of smaller particles spanning 50 km. This more diffuse part of the core is mainly composed of 1–100 μm size particles with a small population of sub-centimeter size particles (Showalter et al., 1992). The several outlying strands, extending over perhaps 150 km radially, are another variable feature, and have changed since Voyager observations. Cassini has detected more than five strands with a much larger radial span compared to the two or three strands detected by Voyager; the strands appear to have a transient, spiral configuration (Charnoz et al., 2005). The core-multistrand structure is itself enveloped in a much broader, 1500 km wide region of much lower optical depth.

In this paper we focus on near-infrared spectra of the F ring obtained by VIMS at high phase angles greater than 177° (Figs. 1 and 2), which means the ring falls near the line connecting the

* Corresponding author.
E-mail address: svahidinia@yahoo.com (S. Vahidinia).

0019-1035/$ - see front matter © 2011 Elsevier Inc. All rights reserved.
doi:10.1016/j.icarus.2011.04.011

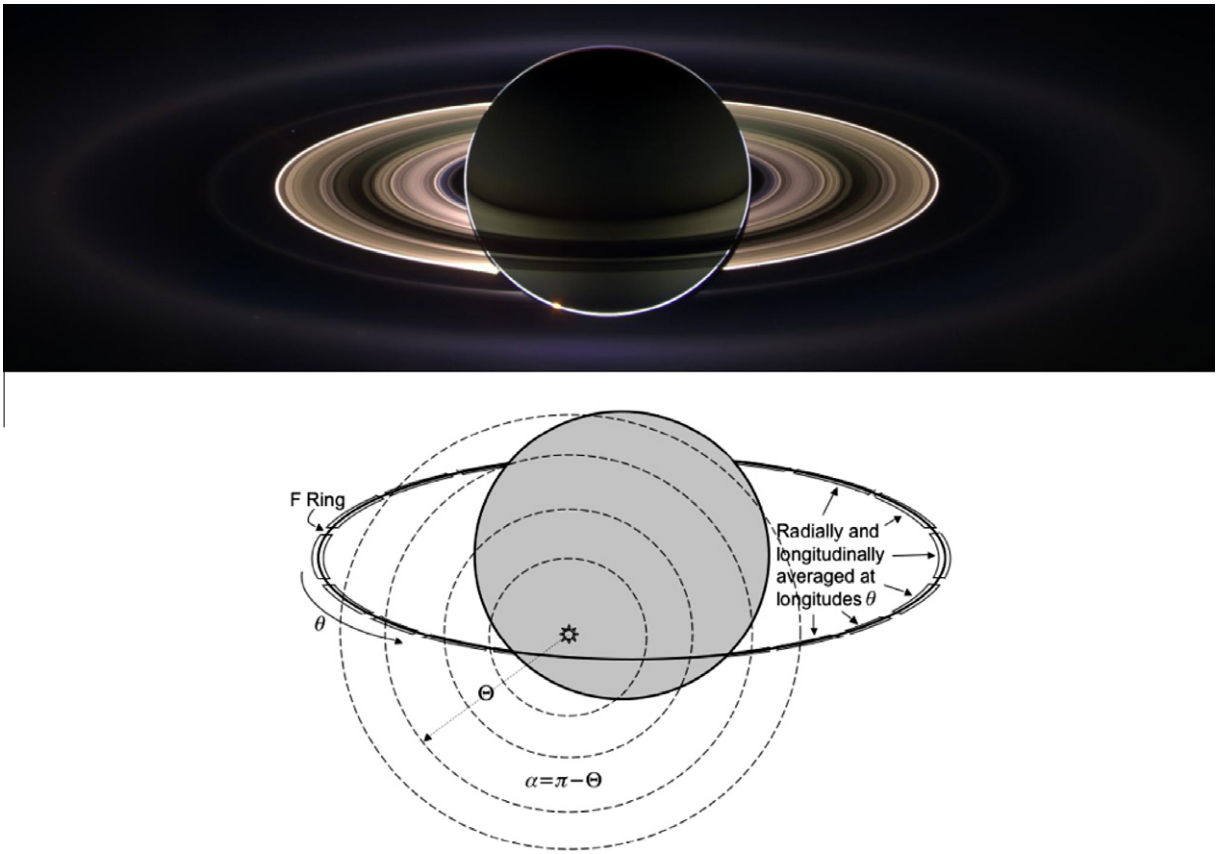

Fig. 1. Illustration of the observing geometry. Top: Cassini ISS image mosaic of the planet and ring system with the Sun in occultation, blocked by the planet. The bright spot on the planet's limb is light refracted through the planet's upper atmosphere, not the Sun itself. The main rings are highlighted by the tiny amount of small, forward scattering dust grains they contain. The diffuse E and G rings are visible at about 2.8 and 4.0 Saturn radii. The F ring is a very bright band lying just outside the main rings. Bottom: The geometry of the VIMS F ring observation, showing the Sun (symbol) behind the planet. Centered on the Sun's direction are loci of constant scattering angle Θ (dashed lines); Θ is an angular offset from the Sun, as seen from Cassini, and the phase angle $\alpha = \pi - \Theta$. Notice that different ring longitudes θ can have the same phase angle α. Because the spacecraft was quite far from Saturn during this observation, Θ was quite small (1–3° for the observations we discuss here). Our spectra came from calibrated VIMS mosaics in this same geometry; we averaged the F ring I/F longitudinally and integrated it radially in bins such as shown (see Section 2).

spacecraft to the Sun. Since the F ring has low optical depth, the observed brightness will be dominated by single-scattered diffraction. Moreover, the observed phase angle falls near the edge of the forward-diffraction lobe of particles of tens of microns radius and typical VIMS wavelengths. VIMS data are an outstanding tool for this type of observation and analysis because of this geometry, their broad spectral coverage (0.35–5 μm), and good spectral resolution. The modeling is somewhat simplified because the particle number density and optical depth are low, so single scattering dominates. In this paper we treat single scattering by two different techniques: Mie theory (assuming spherical particles) and the Discrete Dipole Approximation (DDA) to assess the possibility of irregular aggregates. In our Mie calculations we allow for the effects of porosity using Effective Medium Theory (EMT; Bohren and Huffman, 1983, Chapter 8).

While the forward-scattered light is dominated by diffraction in the ultra-high phase data, we see that the broad spectral trends are interrupted by a narrow dip at 2.87 μm, and the familiar 1.5 and 2 μm absorption features seen at low phase angles are missing (Fig. 3). We can explain both of these spectral surprises in the context of the single scattering diffraction lobe model. The broad peak in the spectra near 2–3 μm wavelength implies a peak in the particle size distribution at sizes around 10–30 μm, as we will show (Section 3.3). Water ice has a Christiansen frequency (real index approaches unity, see Section 3.2) of 2.87 μm, and we find that this is what causes the narrow 2.87 μm dip. We will show that the precise spectral location of the narrow absorption feature (2.87 μm) is a diagnostic of the material (water ice) and even of its crystalline state.

2. Data

The Visual and Infrared Mapping Spectrometer (VIMS) is described in detail in Brown et al. (2004). Briefly, this instrument acquires spectra at 352 wavelengths between 0.35 and 5.2 μm for an array of up to 64 × 64 spatial pixels to produce a map of the spectral properties in a given scene, known as a cube. Two separate channels measure the visual and infrared components of the spectra. The visual (VIS) channel measures spectra at 96 wavelengths between 0.35 and 1.04 μm, while the infrared (IR) channel measures spectra at 256 points between 0.88 and 5.1 μm with a typical spectral resolution of 0.016 μm. In this paper we only consider the IR channel data, for which the angular resolution was 0.5 milliradians.

The data used in this analysis were obtained during times that Cassini flew through Saturn's shadow. While the disk of the Sun was blocked from view, VIMS was able to image the F ring at extremely high phase angles (normally observations are prohibited at phase angles greater than 165° because the remote sensing instruments are not allowed to look too close to the Sun). On day 258 of 2006 during orbit 28, Cassini spent a protracted period of time (several hours) in Saturn's shadow and was therefore able to make extensive observations of the ring system. Two sequences of observations obtained during this time will be considered here.

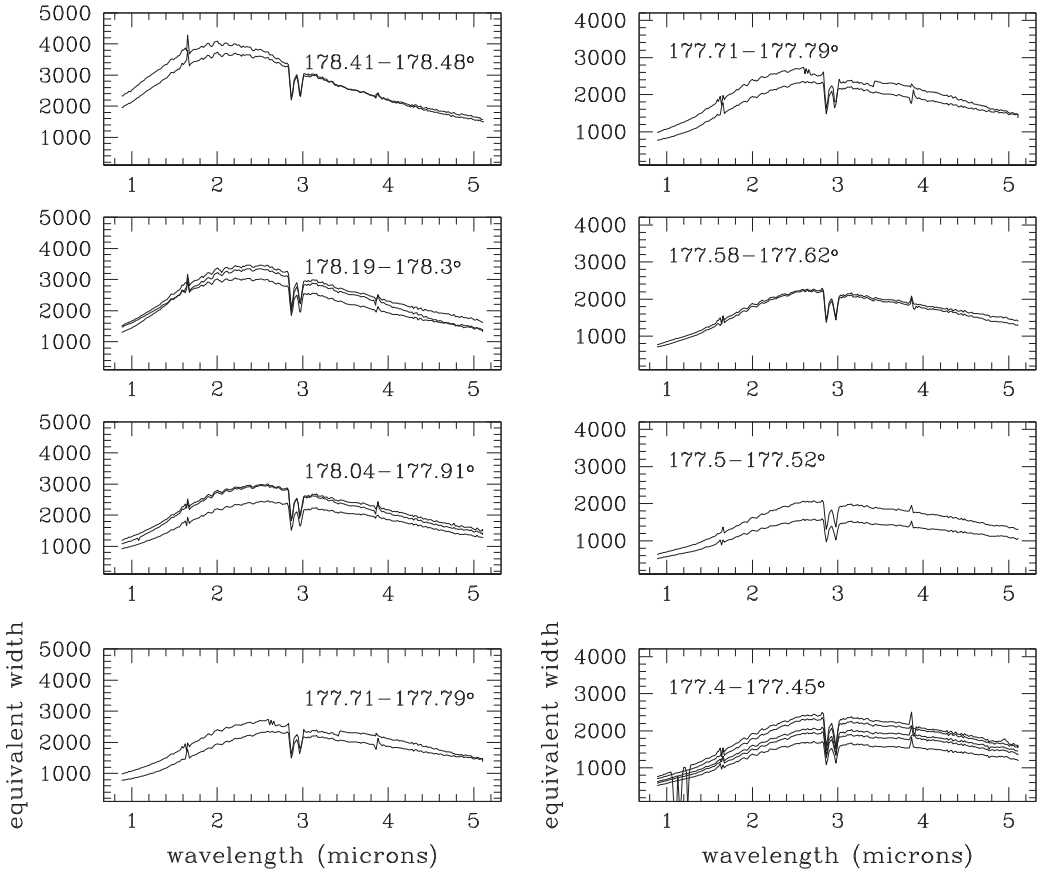

Fig. 2. These panels demonstrate the longitudinal variation of F ring spectra at high phase angles (equivalent width is the radial integral of F ring brightness; see Section 2); the spectra in each phase bin represent different longitudes θ along the F ring having the same phase angle. The spectra in each phase bin are then averaged, since they are all consistent without any gross longitudinal variation in shape. Filter gaps result in three of the four narrow features in the 1–5 μm spectral region with only one being a true spectral signature at 2.87 μm (Section 2.1). Once the anomalous points are removed, we are left with a broad peak from 1 to 5 μm and a single dip at 2.87 μm as seen in Figs. 3 and 4.

The first sequence was named HIPHASE001 and produced a complete mosaic of one ansa of the ring system extending from the planet to outside the core of the E ring. Only the cubes with the shorter integration times are used in this analysis because these were less likely to saturate on the F ring. The second sequence, HIPHNAC, covered both ansae, observing a range of radii and longitudes between the F and D rings. Later, on day 146 of 2007 on orbit 45, Cassini again passed through Saturn's shadow and obtained another series of cubes covering the F ring. Here only five cubes with longer integration times are included in the analysis because the phase angles were not as high as in the orbit 28 data and we wanted to maximize the signal to noise ratio in the F ring.

All the cubes used (listed in Table 1) were calibrated and processed using the standard pipelines to remove dark currents and to convert raw data numbers into the standard measure of reflectance I/F (the pipeline also outputs specific intensity if you desire it), which is unity for a perfect Lambert surface oriented perpendicular to the incident light (McCord et al., 2004; Cuzzi, 1985). The specific calibration curve used with these data was RC17 (technically, RC15 was used to process the cubes, and the final spectra corrected to RC17 using a fixed multiplier at each wavelength). Individual cubes were geometrically navigated based on the available SPICE kernels, and the VIMS pointing was refined based on ring features visible in the individual cubes. This procedure enabled us to determine the observed radius, longitude, phase and emission angle at the ring plane for each pixel in every cube.

The data for each sequence from orbit 28 were then binned onto a grid of radius and longitude values to produce hyper-spectral re-projected mosaics of the rings. The resolutions of these mosaics were 1500 km in radius and 5° in longitude. For each pixel in these re-projected mosaics, we compute the average I/F at each wavelength, along with the mean phase and emission angle. The data from orbit 45 were reduced in a slightly different manner. Here, each cube covered a relatively small range of longitude (15°) but the phase angle changed significantly between cubes. The data from each cube was therefore averaged over longitude to determine the mean brightness versus wavelength on an evenly spaced set of radii. In this case, the radial bins were 100 km wide. Mean phase angles and emission angles were also computed for each radial bin.

In all cases, the result of this step in the analysis was a series of radial profiles, each giving the brightness as function of wavelength and radius for a restricted range of longitudes and phase angles. Each of these profiles was used to compute a single spectrum of the F ring. Since VIMS was unable to resolve the narrow component of the F ring which dominates the brightness in these observations, as seen for instance in higher-resolution images (Fig. 1), we compute a quantity known as the equivalent width W, which is the integrated brightness over a range of radii: $W = \int (I/F)\, dr$, this quantity (which has units of length) has the advantage that it is independent of image resolution, unlike the peak brightness. For the rev 28 HIPHASE001 and HIPHNAC data, the brightness was integrated over a radial range between 138,000 km and 142,500 km from Saturn center. For the rev 45 HIPHASE001 data, a mean background I/F level based on the mean I/F between 143,000 and 150,000 km was first removed from each wavelength

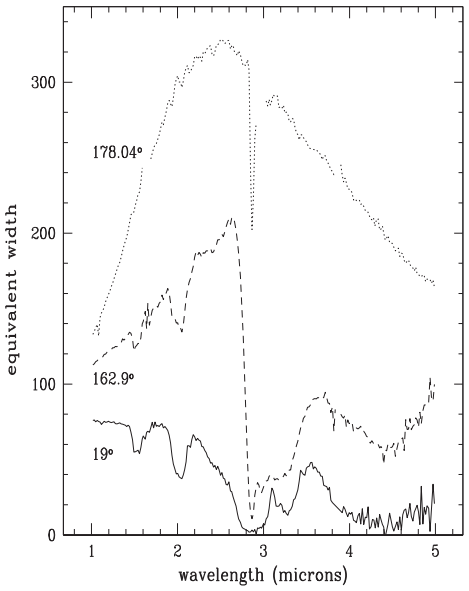

Fig. 3. (Left) Comparison of VIMS spectra at phase angles 178.04°, 162.9°, and 19°. The vertical axis is the equivalent width, or the radial integral of F ring brightness (Section 2). The 1.5 and 2 μm ice bands are clearly present in the lower phase angles, as well as a much wider and deeper 3 μm absorption feature. The high phase angle (178.04°) spectrum has been scaled down by a factor of 9, and the 19° spectrum scaled up by a factor of 30, to display on the same plot. In this paper we deal exclusively with normalized spectra and spectral shapes, so normalization constants are irrelevant.

Table 1
Observations used in this study; each is designated by its observation or "cube" number, taken at some observational mid-time. Each cube has spatial extent given by the pixel dimension (12 × 12, etc.), and the integration time (ms) in both the VIS and IR channels. Only the IR channels are used here.

Cubes	Mid time	Size	Int (IR, VIS)
Rev 28 HIPHASE001			
V1537007144	2006-258T09:57	64 × 64	80, 5120
V1537008474	2006-258T10:09	64 × 64	80, 5120
V1537009791	2006-258T10:41	64 × 64	80, 5120
V1537023251	2006-258T14:23	12 × 12	320, 3840
V1537023308	2006-258T14:24	12 × 12	320, 3840
Rev 45 HIPHASE001			
V1558904277	2007-146T20:28	64 × 48	160, 10000
V1558904798	2007-146T20:37	64 × 48	160, 10000
V1558905900	2007-146T20:55	64 × 48	160, 10000
V1558906421	2007-146T21:04	64 × 48	160, 10000
V1558907125	2007-146T21:17	64 × 32	320, 20000
Rev 28 HIPHNAC001			
V1537020614	2006-258T13:39	12 × 12	320, 3840
V1537020671	2006-258T13:40	12 × 12	320, 3840
V1537020826	2006-258T13:42	12 × 12	320, 3840
V1537020960	2006-258T13:45	12 × 12	320, 3840
V1537021101	2006-258T13:47	12 × 12	320, 3840
V1537021246	2006-258T13:49	12 × 12	320, 3840
V1537021303	2006-258T13:50	12 × 12	320, 3840
V1537022556	2006-258T14:11	12 × 12	320, 3840
V1537022613	2006-258T14:12	12 × 12	320, 3840
V1537022772	2006-258T14:15	12 × 12	320, 3840
V1537022904	2006-258T14:17	12 × 12	320, 3840
V1537023048	2006-258T14:20	12 × 12	320, 3840
V1537023194	2006-258T14:22	12 × 12	320, 3840

channel, and then the residual brightness was integrated over the radial range between 137,000 and 143,000 km. The background-subtraction was done in this case because the observations were at a somewhat lower phase angle so the brightness of the F ring relative to the background was significantly lower. These large radial integration ranges include all the F ring core and strand

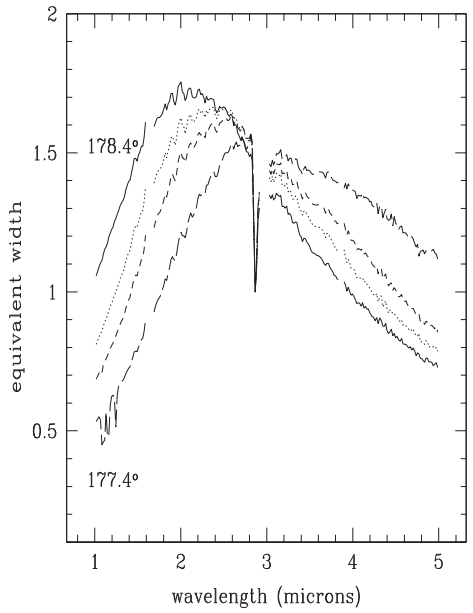

Fig. 4. (Right) VIMS spectra at high phase angles 177.4–178.5°, normalized to their values at 2.87 μm and averaged over longitude in the same phase bin. Note the increasing peak brightness at higher phase angles.

material, plus the 1500 km wide extended halo material. They are both wide enough that the I/F contribution near their edges is negligible, so the fact that they are different is of no interest.

The spectra are very sensitive to phase angle and change drastically in shape and magnitude over a few degrees. Since the F ring is clumpy (i.e., particle number density and optical depth vary; see Section 3.3), we examined the spectra for each phase angle at various longitudes to check for variability (see Fig. 2). The spectra of different longitudes were quite similar in shape at the same phase angle, so we averaged the spectra at different longitudes lying in the same phase angle bin (Fig. 4).

2.1. Filter band gaps

The VIMS spectral coverage is interrupted in three narrow wavelength bands, where the change from one order sorting filter to the next causes a low signal. These order sorting filters reduce overlap between different orders of the grating and block thermal

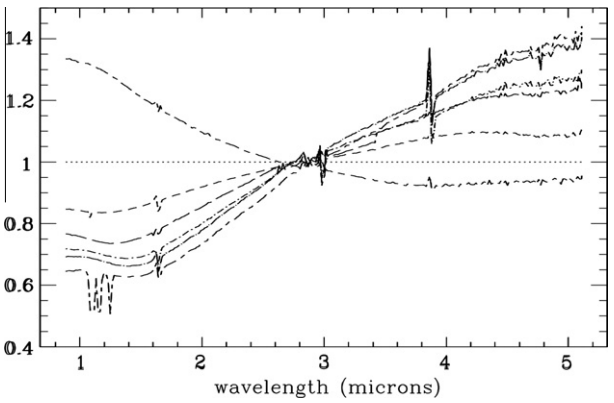

Fig. 5. VIMS spectra of the F ring at different phase angles between 177° and 178° as shown in Fig. 1, ratioed to a single reference spectrum in this range. Only smooth wavelength dependent differences are seen overall, except for noticeable glitches near the three filter band gaps (nominally 1.64 μm, 2.98 μm, and 3.87 μm) and a more subtle glitch near the Christiansen frequency at 2.87 μm.

radiation from the spectrometer optics so as to reduce noise in the long-wavelength (>3 μm channels). In our attempts to remove all possible artifacts from our spectra, we identified and rejected a few channels associated with one of these bands which are usually not rejected by the VIMS team; here we document our reasons for doing so.

Under an earlier version of pipeline calibration (RC15), spectral ripples covered the entire spectrum (these have mostly been removed by the RC17 calibration). In order to understand these, we took ratios of spectra at different phase angles; Fig. 5 shows several of these ratios as functions of wavelength. In the ratio spectra, the worrisome ripples vanished, testifying to their likely instrumental nature and leaving a smooth spectral variation with phase angle which is, however, punctuated by glitches in the regions of the known filter band gaps. Close-up plots of these spectral regions are shown in Figs. 6 and 7, taken from our data sets HIPHASE001 and HIPHNAC respectively. These are doubly normalized spectral plots. After being normalized as above (ratioed to one selected spectrum in our phase angle range 177.4–178.5), they are next normalized by one of their own (normalized) spectral intensity ratios. The 2.87 μm Christiansen frequency (Section 3.2) shows localized variations, but they are spread over several channels in a systematic way, and vary smoothly with phase angle (the three ratios in Fig. 7 which sharply decrease to shorter wavelengths connect to saturated points which were designated as zero, so are artifacts). The 2.87 μm feature is well away from any filter gaps, and we believe it is real.

The three known filter gap regions all show similar behavior: strong bin-to-bin variations which are not always smoothly or systematically varying with phase angle. These glitches are seen across a well-defined range of wavelengths, but are not generally

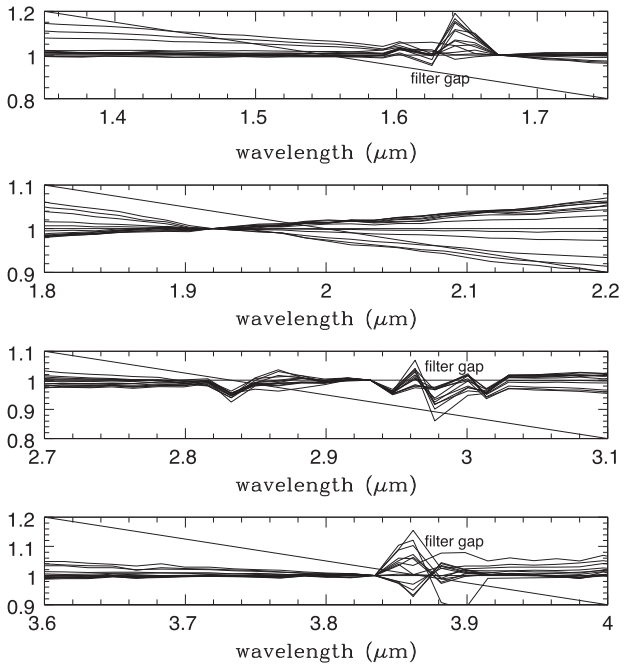

Fig. 6. Expanded and doubly normalized plots of spectral regions of possible interest at different phase angles (see Section 2.1), first normalized as in Fig. 5 above, and then again at a selected wavelength in each spectrum. Four spectral regions are shown: the second panel shows the water ice 2 μm band region – no glitch at all can be seen. The top panel and bottom two panels show regions near the known filter band gaps. The 2.87 μm Christiansen feature (2.82–2.90 μm) can be seen to vary slightly with phase angle, but at an even lower level than the regions near the filter band gaps. In this figure the 1.6 μm and 3.8 μm filter band gaps are seen to affect four spectral channels each and the 2.9 μm filter band gap is seen to affect five channels. This figure shows the HIPHASE001 data set.

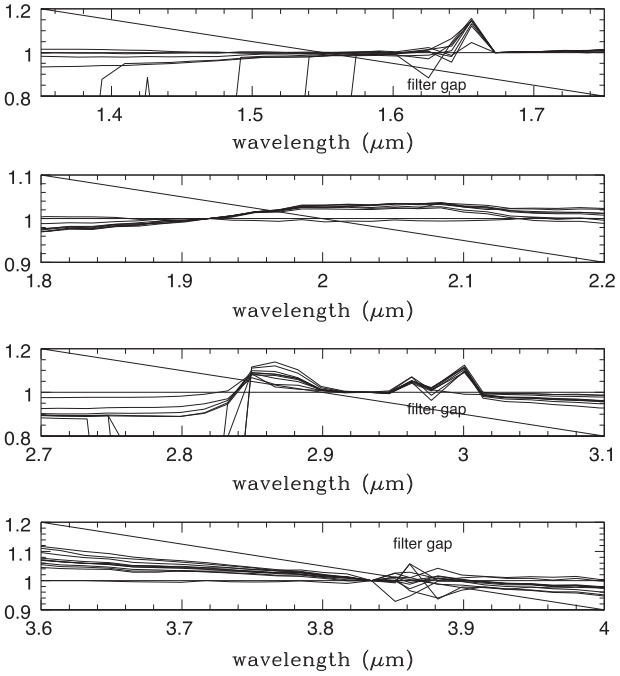

Fig. 7. Same as Fig. 6 but for the HIPHNAC data set.

restricted in their contamination effects to only three wavelength bins (the nominal gap channel and two adjacent channels). In the (slightly) lower phase angle series from HIPHNAC (Fig. 7), one might identify only three corrupted bands in two of the three filter band gaps (1.62, 1.64, 1.65 μm; 2.96, 2.97, 3.00 μm). However, in the HIPHASE001 series (Fig. 6), four or even five wavelengths are corrupted in all cases (1.60, 1.62, 1.64, 1.65), (2.94, 2.96, 2.97, 3.00, 3.01), (3.85, 3.86, 3.88, 3.90), and by comparison it seems to us that the HIPHNAC data (Fig. 7) may be corrupted in the same four channels of the 3.87 μm filter gap, as well. For this reason we would prefer not to assign any observational significance to data in any of these broader regions. The VIMS team traditionally rejects at most three channels: the nominal filter gap wavelength and the two adjoining wavelengths. This approach results in F ring spectra apparently containing *two* sharp dips in the 3 μm spectral region (Fig. 2; also see Cuzzi et al., 2009; Nicholson et al., 2008). While there is no known reason to expect corruption of the four or five channels where we see what appears to us to be suspicious behavior, the above discussion suggests to us that the longer-wavelength sharp dip seen at 2.95–3.01 μm in the VIMS high-phase F ring spectra shown in Fig. 2 is not real, and we disregard it from our plots and analyses.

3. Modeling

We model the F ring particles as solid spheres, porous spheres, non-spherical solid particles, or non-spherical aggregates. The model consists of a size distribution, which represents the size of a typical ring particle, the composition of the particles as described by their optical constants (Sections 3.1 and 3.2), and the internal structure of the particle as modeled three different ways: (a) solid, (b) porous but on such a small scale that structure is irrelevant; or (c) porous but composed of monomers with size comparable to the VIMS wavelengths. The first two kinds of particle internal structure can be handled by Mie scattering combined with Effective Medium Theory (EMT; Section 3.3) or by standard irregular particle theories based on Mie scattering (e.g., Pollack and Cuzzi, 1980). We did not use this latter approach here; see Hedman et al., 2009) for a similar

approach using Fraunhofer diffraction to approximate near-forward scattering. The final possibility (c) requires more sophisticated modeling, and for this we used the Discrete Dipole Approximation (DDA). While the DDA is also capable of modeling inclusions of different composition, we do not feel it is justified by the observations at this stage. We can start constraining the particle size distribution, composition, and porosity with the simpler Mie theory and EMT model (Section 3.3) before moving on to the more complicated discrete dipole model (Section 3.4).

3.1. Optical constants

All scattering calculations use optical constants or refractive indices for the particles of interest; we selected the best data set for our purposes. We assume that the F ring particles are composed mostly of water ice for which optical constants (real and imaginary refractive indices n_r and n_i respectively) are known to vary over the temperature range in question. We will further assume the ring particle temperature to be 100 K (Esposito et al., 1984) and thus will use optical constants valid at this temperature. There are various optical constant data sets that cover water ice at 100 K in the near infrared. We considered data for crystalline and amorphous ice from Hudgins et al. (1993), Leger et al. (1983), Bertie (1969), Bertie and Jacobs (1977), and Mastrapa et al. (2008, 2009). Data from Hudgins et al. (1993) and Leger et al. (1983) are for amorphous ice and data from Bertie and Jacobs (1977) are for crystalline ice. Mastrapa et al. (2008, 2009) has the most recent data set for both crystalline and amorphous ice at various temperatures (Fig. 8). This data set is also more finely sampled in wavelength, which results in better modeling of the spectrum. Mastrapa et al. (2008, 2009) obtains the optical constants of ice by measuring the absorption coefficient ($4\pi n_i/\lambda$) through a thin film of ice. These measurements have been done in two separate experiments from 1.1 to 2.6 μm and 2.5 to 22.0 μm. Since we need optical constants from 1 to 5 μm, it is important to have the constants in that range without any discontinuities. For instance, an artificial discontinuity in the ice optical constants near 2.9 μm might have corrupted the model spectra of Poulet et al. (2003) to some degree (F. Poulet, personal communication, 2007). We combined the two data sets by using a Kramers–Kronig analysis on the imaginary index (obtained from the absorption coefficient) of the spectrum to calculate the real refractive index as a function of λ. Mastrapa's data is taken in two independent wavelength regimes, and the results are not the same at overlapping wavelengths in both data sets. To perform a KK analysis, one must bridge the two data sets using some smooth function. The function we adopted was slightly different from the function adopted by Mastrapa et al. (2009), leading to small differences in the inferred values of (n_r, n_i) in the transition region. In Fig. 8 we compare our results with those from Mastrapa et al. (2009). This comparison shows that any systematic error in n_r is extremely small. This is small because the 3 μm band is so strong; the analysis basically tries to capture the largest features in the spectrum, and minor perturbations in lower values of the imaginary index are not contributing factors to the real index. The 3 μm band is due to O–H stretching and is composed of two separate components (ν_1 and ν_3), where ν_1 corresponds to the symmetric O–H stretching and ν_3 to the asymmetric O–H stretching (Ockman, 1958; Hornig et al., 1958).

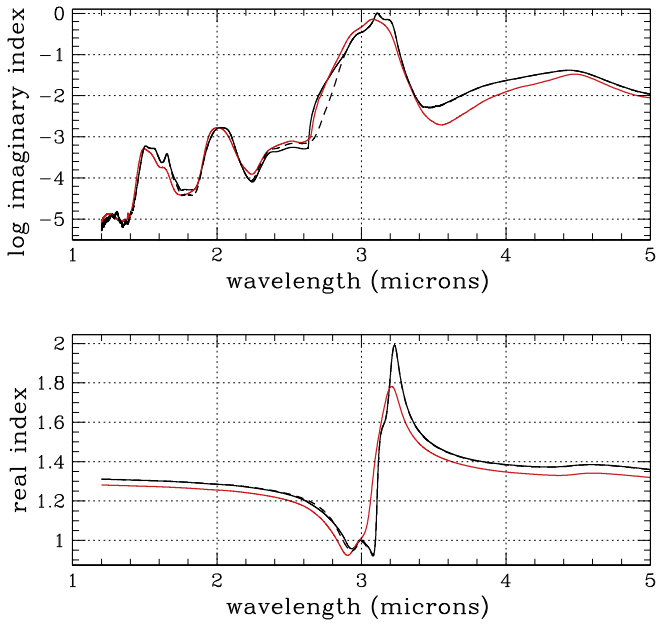

Fig. 8. Optical constants for crystalline ice at 100 K (Mastrapa et al., 2008, 2009) (black) and amorphous ice at the same temperature (red). Two independent Kramers–Kronig analysis with different bridging functions are shown in solid black (our analysis, see Section 3.1) and dashed black (Mastrapa et al., 2009). The crystalline ice real index begins to approach unity at 2.8 μm and first crosses unity at 2.88 μm (real index from Mastrapa's analysis crosses unity at 2.87 μm), whereas the amorphous real index crosses unity at a shorter wavelength, closer to 2.83 μm. (For interpretation of the references to color in this figure legend, the reader is referred to the web version of this article.)

3.2. Christiansen frequency physics

The water ice 3 μm band is interesting because the real part of the refractive index n_r crosses unity multiple times between 2.8 and 3.1 μm. The implications of this have been discussed by multiple authors (Conel, 1969; Arnott et al., 1995; Mustard and Hays, 1997); a frequency where $n_r = 1$ and $n_i \ll 1$ is referred to as a Christiansen frequency. Under these conditions, external reflection and refraction by the particle are negligible and an impinging wave propagates straight through the particle. If pure absorption within the particle is also small ($\sim 4\pi n_i/\lambda \cdot 2r \ll 1$) the wavefront is only minimally disturbed and, by Huygens' principle, extinction of the wave is minimal. Thus for a diffraction dominated spectrum at high phase angle (due to wavelength-sized particle contributions), the intensity scattered to some small angular distance from direct forward scattering *decreases* at the wavelength where $n_r = 1$ (as observed in the F ring spectrum at 2.87 μm). There are multiple wavelengths between 2.8 and 3.1 μm, where $n_r = 1$, but we only see one dip in the spectrum. This is because at the longer wavelength Christiansen frequencies (near 3 μm) the value of the imaginary index itself is large enough that it alone provides both significant external reflection and internal absorption, so by Huygens' principle can contribute to disturbance of the incident wavefront and normal extinction.

For the same reason, the Christiansen frequency phenomenon results in an *increase* in the directly transmitted light at this same wavelength, as was observed by Cassini's VIMS during solar and stellar occultations (Nicholson et al., 2007; Hedman et al., 2011). This effect is complementary to the decrease in near-forward diffraction and its analysis leads to conclusions similar to those presented here.

3.3. Basic radiative transfer for a diffuse ring layer

This section outlines important radiative transfer concepts used in our Mie–EMT modeling described in Section 3.4 and DDA modeling described in Section 3.5. Modeling the F ring as a homogeneous layer of normal optical depth τ, containing N particles with radii r, we calculate the observed I/F as a function of the single particle Mueller scattering matrix **S**. The Mueller matrix elements

relate the Stokes parameters (parameters defining the intensity and state of polarization) of incident and scattered light (this matrix is called F_{ij} in Van de Hulst (1957, from here on referred to as vdH) and (Hansen and Travis, 1975), from here on referred to as HT)); note below however, they use different conventions for "intensity". For incident unpolarized light, the first Mueller matrix element S_{11} defines the scattered light and will be used in our calculations (see Eq. (1)). The derivations of vdH (Section 2.1) and HT (Section 2) relate what we refer to as the flux density F_s (erg cm^{-2} s^{-1}) scattered by a single particle, as seen at distance R and direction (θ,ϕ), to the incident flux density which we denote as πF: (see also Eq. (4) below)

$$\frac{F_s}{\pi F}=\frac{S_{11}}{k^2R^2} \tag{1}$$

We reserve the term intensity for flux density per unit solid angle ((Chandrasekhar, 1960); see also HT Section 3). For a scattering system such as a ring, consisting of a volume of N scatterers of radius r, having a finite angular extent $d\Omega$ as seen by the observer, the traditional quantity of interest is the intensity I or flux per unit solid angle. Moreover, remote observations normally express the brightness of an extended source as its reflectivity or the ratio of its intensity to the intensity from a perfect Lambert surface, illuminated and viewed at normal incidence, covering the same solid angle, which is $I_L = \pi F/\pi = F$. We thus rewrite Eq. (1) to address an optically thin layer of scatterers with area A normal to the incident flux and vertically integrated particle surface number density N/A. Viewed by the observer at an angle θ from the normal to A, where $\mu = cos\theta$, the solid angle subtended by the scatterers is $d\Omega(A,R) = \mu A/R^2$, and the scattered intensity for the particle layer is:

$$I_s(r)=\frac{NF_s}{d\Omega}=\frac{\pi FS_{11}N}{\mu k^2A} \tag{2}$$

For a distribution of particle sizes, $\frac{N}{A}=n(r)dr$, where the particle number density $n(r)$ is an area density per unit particle radius equal to n_0r^{-p} for a differential power law particle size distribution. The Intensity for the layer is then summed over the particle size distribution to get the total scattered intensity (expressed as I/F):

$$\frac{I}{F}=\sum_{r_{min}}^{r_{max}}\frac{\pi S_{11}}{\mu k^2}n_0r_i^{-p}\Delta r_i \tag{3}$$

The scattered flux for a single particle can also be expressed in terms of its standard scattering phase function $P(r)$:

$$F_s=\frac{\pi F\sigma_{sca}(r)P(r)}{4\pi R^2} \tag{4}$$

We can use Eqs. (2) and (4) to relate S_{11} to the phase function $P(r) = 4\pi S_{11}(r)/k^2\sigma_{sca}(r)$, where P, like S_{11}, is a function of scattering angle from the incident direction and particle properties (refractive indices and particle radius r), $k = 2\pi/\lambda$, and scattering cross section $\sigma_{sca}(r)$. The dimensionless efficiency factors for scattering, absorption, and extinction by the particle of size parameter $x = 2\pi r/\lambda$ at wavelength λ are $Q_s(r)\equiv\sigma_{sca}(r)/\pi r^2$, $Q_a(r)\equiv\sigma_a(r)/\pi r^2$, and $Q_{ext}(r)\equiv Q_a(r)+Q_s(r)$.

Substituting Eq. (4) for F_s in Eq. (2), the scattered intensity for a volume of N scatterers can be expressed in terms of $P(r)$:

$$I_s=\frac{NF_s}{d\Omega}=\frac{N\pi F\sigma_{sca}(r)P(r)}{4\pi\mu A}=\frac{FP(r)\varpi(r)d\tau(r)}{4\mu} \tag{5}$$

where single particle albedo $\varpi(r) = Q_s(r)/Q_{ext}(r)$, and the increment of optical depth is defined as $d\tau(r) = n(r)Q_{ext}(r)\pi r^2dr$. Summing over the particle size distribution we get the total scattered intensity, expressed as I/F:

$$\frac{I}{F}=\varpi P\frac{\tau}{4\mu}=\sum_{r_{min}}^{r_{max}}\frac{\pi S_{11}(r)}{\mu k^2}n_0r_i^{-p}\Delta r_i \tag{6}$$

where now ϖ, P, and τ are understood to be averaged over the particle size distribution at wavelength λ. The two expressions in Eq. (6) for I/F will be used in our modeling in Sections 3.4, 3.5, and 3.6. Also, we are primarily interested in calculating the shape of the spectrum rather than the absolute value of I/F, since the F ring's optical depth is difficult to measure because it is highly variable with longitude and time.

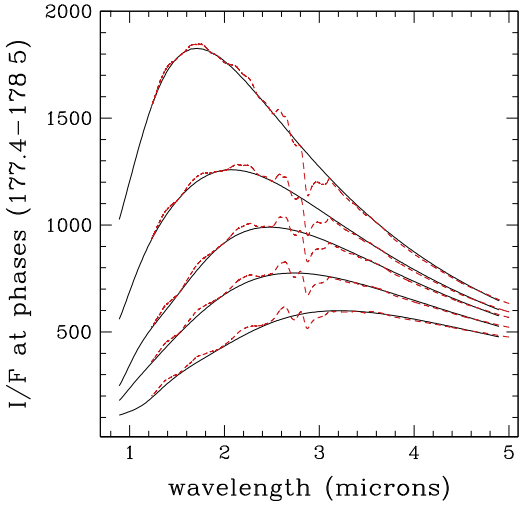

Fig. 9. (Left) I/F for solid carbon particles (black) and solid crystalline ice particles (red) calculated with a Mie model for the same size distribution (10–30 μm power law) and phase angles ranging from 177.4° to 178.5°. The overall spectral shapes for both disparate compositions match very well except for the 2.87 μm dip present in the ice spectrum. (For interpretation of the references to color in this figure legend, the reader is referred to the web version of this article.)

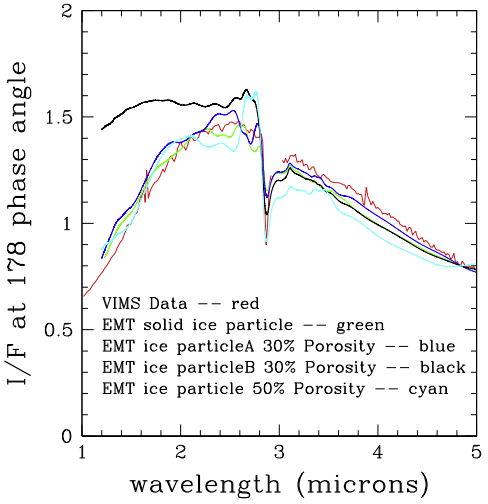

Fig. 10. (Right) Comparison of VIMS data and Mie–EMT models for crystalline ice particles with different porosities and no internal structure at one phase angle (178°). All the Mie–EMT calculations in this plot have been done with a power law particle size distribution ranging from 10 to 30 μm, except for the Mie–EMT particle (solid black) which was done for a broader size distribution (5–30 μm), and clearly demonstrates the effect of smaller particles on the fit. Solid ice has the best overall fit, but the band depth is too shallow compared to the data. As the porosity increases, the band depth also increases, but at the expense of the overall fit.

3.4. Mie scattering and diffraction

We start with the simplest scenario, in which the ring particles are assumed to be spherical ice particles of uniform but arbitrary density (depending on their porosity), assuming internal structures are much smaller than the wavelength λ, so particles look isotropic and homogeneous to the wave. Mie theory (or even simple diffraction theory; (Hedman et al., 2009) can be used to calculate scattering from such particles after refractive indices are calculated which are appropriate for the desired porosity (see below in Section 3.4.1 for how porosity was treated).

The overall spectral profiles at high phase angle are dominated by the diffracted component of the scattered light in the forward direction (Pollack and Cuzzi, 1980; Hedman et al., 2008). The dominance of diffraction at high phase angle is demonstrated by comparing the spectrum of absorbing carbon particles to that of solid ice particles with the same power law size distribution (Fig. 9). The overall profile of the carbon spectrum must be due to diffraction only, since carbon has negligible contribution to scattering from external reflection and its absorption coefficient is so large that no internal transmission/refraction takes place. Therefore, absorbing particles only diffract light in the near forward direction. The "red" slope at shorter wavelengths (brightness increases with λ) is caused by a deficit of smaller particles ($r < 10$ μm) needed to contribute to diffraction at shorter wavelengths at this phase angle, which brings down the intensity at that end. Recall that the width of the diffraction lobe is $\sim\lambda/2r$, thus for some fixed angular offset $180 - \alpha$ from the forward direction, $\lambda/r \sim$ constant. Similarly, at longer wavelengths, the "blue" slope (brightness decreases with λ) is caused by a deficit of large particles ($r > 30$ μm). Applying this simple model to solid ice particles with particle radii between 1 and 40 μm, we found that the envelope of the F ring spectrum requires a limited width size distribution, which we modeled as a power law (r^{-3}) with radii $r \approx 10$–30 μm (see also Hedman et al., 2008). The interesting aspect of this result is that the distribution is somewhat narrow compared to most diffuse ring distributions except the E ring (see Showalter et al., 1991; Throop and Esposito, 1998); our approximation by a power law instead of a smooth, unimodal distribution such as Hansen–Hovenier distribution (HT Section 2), for instance, may be refined in future studies and is likely not of significance over this narrow size range.

In Fig. 9 the overall profile of the ice and carbon spectra for the same particle size distribution follow the same pattern at various phase angles. This demonstrates that, like the carbon particles, the ice particle spectra are also dominated by diffraction. The carbon particles, of course, do not display a Christiansen feature in this spectral range. Realizing that the scattered light is dominated by diffraction makes it easy to understand the absence of the familiar 1.5, 2.0, and 3 μm features seen at lower phase angles (Fig. 3) the amount of light that has entered the ice particle is merely a small perturbation on top of the large diffracted component. This is because the transmitted light, whether absorbed or not, is dispersed by refraction into a far larger solid angle than the diffracted component (HT Fig. 5).

There is clearly some spectral manifestation of the strong 3 μm water ice band, but the shape and even central wavelength of the observed feature are unusual. Its shape is extremely narrow and its central wavelength is at significantly shorter wavelengths than the peak absorption in the ν_3 band (at 3.1 μm). It looks nothing like the 3 μm absorptions seen at lower phase angles (Fig. 3). This narrow feature is due to the Christiansen effect at 2.87 μm, where the real index crosses unity and extinction drops significantly (see Sections 3.2 and 3.6). We find that the two major features of the F ring spectrum – the spectral envelope, which represents only the particle size distribution, and the 2.87 μm dip, which is the only manifestation of the optical properties – can be modeled separately. In Section 3.5 we describe our modeling of the 2.87 μm feature.

3.4.1. Porous particles analyzed by effective medium theory

Our first models, using solid water ice, failed to give a dip at 2.87 μm that was as sharp and deep as the data (see Fig. 10, green curve). Next, we used Effective Medium Theory (EMT) to model porous particles to see if porosity would affect the depth and shape of the 2.87 μm band, while leaving the overall spectral envelope unchanged. EMT calculates effective optical constants for a composite/porous particle by averaging over its constituents. There are various flavors of EMT (Bohren and Huffman, 1983); our calculations use Maxwell Garnett theory where the average refractive

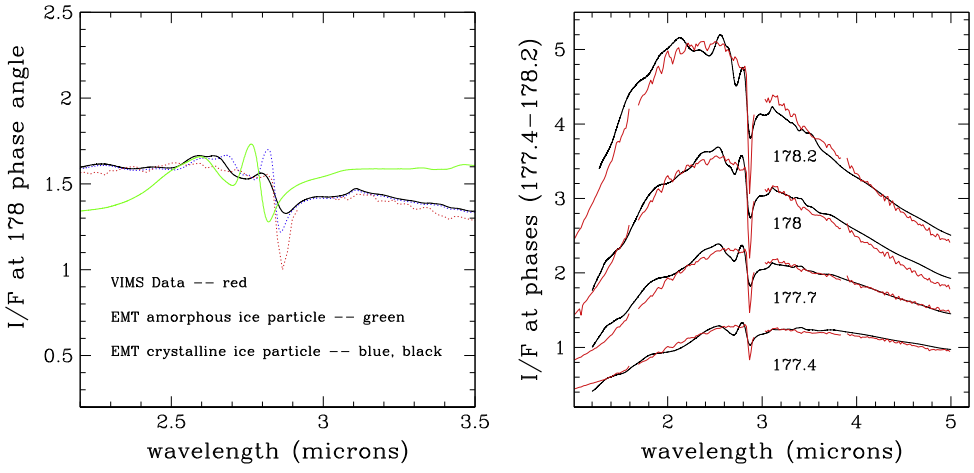

Fig. 11. (Left) Mie–EMT calculations show the crystalline ice Christiansen feature, positioned at 2.87 μm, matching the observed position of the feature in the VIMS data. The EMT spectrum in black has been calculated using our *k*–*k* analysis of Mastrapa's optical constants data, and spectrum in blue was calculated using Mastrapa's *k*–*k* analysis. There is a slight difference between the Christiansen feature's position, width, and depth using Mastrapa's *k*–*k* analysis (narrower width, deeper, and positioned at 2.865) and our *k*–*k* analysis (larger width and positioned at 2.87). This comparison gives us an idea of the systematic error introduced in these calculations from different bridging functions between the optical constants data sets (see Section 3.1). From here on we will use our *k*–*k* analysis of Mastrapa's optical measurements for the rest of the calculations. The amorphous ice feature occurs at a shorter wavelength (2.82 μm) than observed and does not agree with the observed spectrum as well. (Right) VIMS spectra (red) and EMT ice particles with 30% porosity (black) at various phase angles ranging from 177.4 to 178.2°. The size distribution used for fitting the spectra at phase angles 177.4–178.0 is our standard power law ranging between 10 and 30 μm (Section 3.4). Improved fits to spectra at the highest phase angles (178.2°) requires a slightly narrower size distribution such as 12–30 μm particle radii to properly fit the short wavelength end. Such a small variation of $n(r)$ with longitude is not implausible (see Fig. 2). (For interpretation of the references to color in this figure legend, the reader is referred to the web version of this article.)

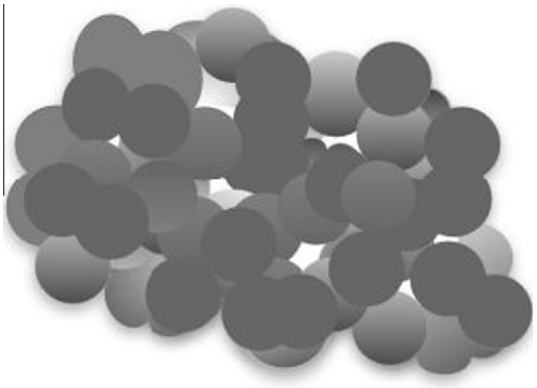

Fig. 12. Simulated aggregate (radius 15 μm and 30% porosity) with overlapping monomers of radii r_m. We have explored r_m between 1 and 3 μm here and in the models of this paper $r_m = 3$ μm. The idealization of a single monomer size is diminished because the overlapping monomers form a lumpy aggregate with a range of effective monomer sizes and shapes.

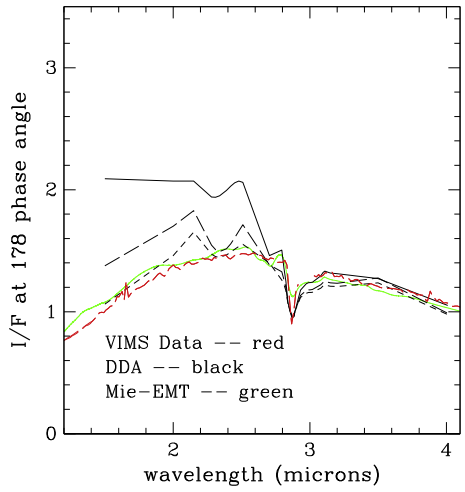

Fig. 13. F ring VIMS data (red) modeled with: Mie–EMT crystalline ice particles with a power law size distribution ranging between 10 and 30 μm in radius and 30% porosity (green), DDA crystalline ice aggregates (black) with the same porosity and three different size distributions. The DDA power law size distributions range between 9.5 and 33 μm in aggregate radii (solid black), 11.5 and 33 μm (long black dash), and 12.5 and 33 μm (short dash). (For interpretation of the references to color in this figure legend, the reader is referred to the web version of this article.)

index of a porous particle is calculated by assuming that its solid component contains unresolved vacuum sites or, *vice versa*, small spherical solid particles are distributed in a vacuum "matrix". The amount of vacuum (porosity) is a free parameter in the calculation and we tested scattering for various porosities. We define the solid volume fraction as f and the porosity as $1 - f$. A simple way to visualize the effects of porosity on scattering is to consider a simple linear expression for the volume-weighted average of the indices which is valid in cases where $|n_r - 1| \ll 1$ and $n_i \ll 1$ with the complex refractive index $m = n_r + in_i$ (Van de Hulst, 1957, Chapter 11), as is true for our spectral range of interest (Cuzzi and Estrada, 1998). Since $n_i(\text{porous}) = f \cdot n_i$, and $n_r(\text{porous}) = 1 + f \cdot (n_r - 1)$, porous particles have n_r closer to unity which causes the extinction efficiency Q_{ext} to be dominated by absorption through the particle. In this regime where $x \gg 1$ and $|m - 1|x \gg 1$, anomalous diffraction theory can be used to get an analytic formula defining Q_a, Q_s, and Q_{ext} (Draine and Allaf-Akbari, 2006) which we will use to motivate a toy model of the process (Section 3.6). Fig. 10 shows calculated water ice spectra for different porosities; higher porosity caused the 2.87 μm band to get too deep and wide in a relative sense, since it caused the particle albedo and Q_{ext} to increase well away from the 2.87 μm dip.

The simple Mie model was useful to constrain the particle size distribution at ultra high phase angles (see Fig. 11) and explain the location and uniqueness of the 2.87 μm feature. In Fig. 11, we can see that the position of the 2.87 μm dip is better fit by crystalline ice, whereas the amorphous ice spectral dip shifts to a shorter wavelength with respect to the data and crystalline ice. The Mie–EMT approach helped us understand the effects of porosity on the spectrum but it failed to match the 2.87 μm band shape qualitatively or quantitatively, so we move on to a different approach (the Discrete Dipole Approximation or DDA) where we assume that the ring particles are aggregates instead of single spherical particles.

3.5. Discrete Dipole Approximation (DDA)

The Discrete Dipole Approximation (DDA) is a brute force method, originally introduced by Purcell and Pennypacker (1973); we will utilize the version developed by Draine and Flatau (1994). The DDA is a method of calculating the scattering and absorption of electromagnetic waves by a target object of arbitrary geometry. Target objects are constructed from a regular lattice of individual polarizable dipoles with size smaller than a wavelength (λ) so that the target mimics a homogeneous dielectric material. The dipole spacing is restricted by the criterion $|m|kd \leqslant 1$, where m = complex refractive index, $k = 2\pi/\lambda$ is the wavenumber, and d = dipole spacing (this forces the optical path length $2\pi md$ to be less than the wavelength λ, and the dipoles act as point scatterers). The polarizability of each dipole can be adjusted to represent the refractive indices of different materials. The polarization state of all dipoles in the system is iterated in response to their individual scattered fields, until a steady state solution is obtained. The overall scattering and absorption cross sections of the array of dipoles are calculated from the final dipole polarization solution. The scattered intensity is calculated from the Mueller Matrix elements S_{ij} obtained from the DDA code (see Section 3.3, Eq. (3)). We define the porosity Φ of our aggregates by using the method of moments developed by Shen et al. (2008),

$$\Phi = 1 - f, \tag{7}$$

$$\text{filling factor } f = (\alpha_2 + \alpha_3 - \alpha_1)(\alpha_3 + \alpha_1 - \alpha_2)(\alpha_1 + \alpha_2 - \alpha_3)^{-1/2} \tag{8}$$

where $\alpha_i = I_i/0.4Ma_{eff}^2$, and I_i is the aggregate's moment of inertia for principal axis i. The radius of a solid, equivalent mass sphere $a_{eff} = r \cdot f^{1/3}$ and the number of dipoles in the aggregate is $N_d = (4\pi/3)(a_{eff}/d)^3$.

From our EMT modeling we find that we need aggregate radii r between 10 and 30 μm with an optical size $x = 2\pi r/\lambda$ ranging from 12 to 33 at 2.0 μm wavelength. The aggregates are composed of individual monomers ranging between 1 and 3 μm in radius r_m (see Fig. 12). The DDA model has recently been optimized by consultants at NASA's HEC Computing facility at Ames Research Center to be able to handle large scatterers such as our aggregates ($2\pi r/\lambda \simeq 100$). The optimized code (http://www.astro.princeton.edu/~draine/DDSCAT.7.0.html) uses a combination of MPI and OpenMP, where loops within the code are spread out among multiple CPUs. The consultants obtained time improvements of about 20 times over the unparallelized version (DDSCAT6.0), and we run on a fast system using typically 64 CPUs.

The aggregates are simulated by first picking the desired aggregate envelope size from the size distribution constrained by the Mie–EMT model, a porosity, and a monomer radius r_m. The monomer centers are selected randomly within a sphere of radius r_{agg} and assigned radii; the ensuing spherical monomers can overlap

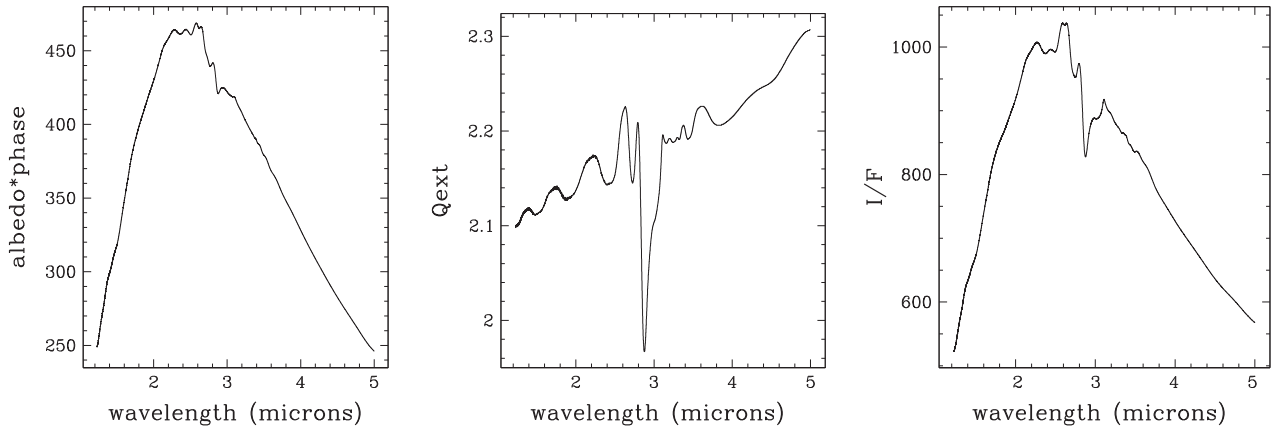

Fig. 14. I/F is the product of phase function P, extinction coefficient Q_{ext}, and albedo ϖ. The left segment is the product of ϖ and P, with Q_{ext} in the middle, and finally the product of all three parameters giving the normalized intensity I/F in the last segment (plots from Mie–EMT runs). The major effect on the depth of the band in the spectrum is from Q_{ext}.

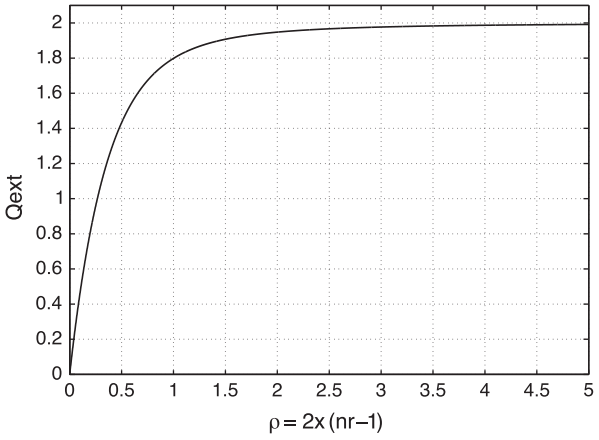

Fig. 15. Extinction coefficient Q_{ext} versus phase shift $\rho = 2x(n_r - 1)$, where n_r is the real refractive index, and size parameter $x = 2\pi r/\lambda$. The expression used to plot Q_{ext} here is valid in the ADT regime and is for an absorbing particle with $n_r = 1.02$ and $n_i = 0.08$ (values close to those at the Christiansen frequency at 2.87 μm). As we approach the Christiansen frequency, $\rho = 2x(n_r - 1) \ll 1$, where Q_{ext} is monotonically increasing.

so, even though r_m is constant for an aggregate, a degree of lumpiness or irregularity is present (Fig. 12). We fill the aggregate with such monomers until the desired porosity Φ is reached. We explored $r_m = 1$–3 μm, which produced little difference, and settled on $r_m = 3$ μm. The aggregate is then populated with dipoles which reside on a regular grid in (x,y,z) and fill the volume stipulated by the placement of the monomers. The dipole size needed to satisfy the DDA criteria $mkd = 1$ is calculated. We have not done convergence tests but since we are primarily interested in integrated quantities such as Q_e, rather than details of, for instance, the polarization or phase function, $mkd = 1$ will be satisfactory for our calculations. The scattering calculations are averaged first over a series of 32 orientations for a given realization of an aggregate, then over alternate realizations of the monomers within the same size aggregate, and finally over a size distribution of similarly averaged aggregates.

Fig. 13 shows the results from DDA aggregates using three different size distributions and 30% porosity, compared to a Mie–EMT calculation of similar porosity and to VIMS data at 178° phase angle. The DDA size distribution is coarsely binned using 10–12 aggregate sizes. The noisy oscillations at wavelengths shorter than 2.87 μm are due to coarse size sampling and diminish as more size bins are used. The Christiansen feature band depth modeled with this approach is a much closer match to the VIMS data. However, the overall spectral fit is degraded at short wavelengths when the same size distribution as that of Mie–EMT modeling is used. Adjusting the size distribution to contain fewer small particles brings down the short wavelength end of the spectrum (see Fig. 13) but simultaneously widens the 2.87 μm band somewhat. Further refinements of the model involving size binning, porosity, monomer sizes or size distributions, etc. might be profitably pursued, but the DDA models are quite lengthy to run and we feel at this point that the aggregate model is on the right track. The difference between the Mie–EMT and DDA aggregate fits (band depth and size distribution) can be explained by a simple toy model, described in the next section.

3.6. Toy model

In this section we describe a simple model which helps explain the difference between the DDA and Mie–EMT results, especially in the wavelength region where $n_r \sim 1$. Specifically, the depth of the Christiansen feature is much shallower for the Mie–EMT model than for DDA aggregates, and the size distributions needed to fit the overall shape of the spectrum are different between the two models.

To motivate the model we first separate the net scattering behavior of the particles into three somewhat differently behaving functions. We rewrite the integrated quantities of Eq. (6) as

$$\frac{I}{F} = \varpi P \frac{\tau}{4\mu} = \frac{\varpi P Q_{ext}}{4\mu} \sum_{r_{min}}^{r_{max}} \pi r^2 n(r) \Delta r_i, \tag{9}$$

where Q_{ext} is also a size-integrated average extinction efficiency. We can separately explore the dependence of ϖ, P, and Q_{ext} on wavelength for any size distribution (Fig. 14). Looking at the components of the scattered field we can see that the extinction efficiency Q_{ext} is the major contributor to the shape of the Christiansen feature, and also has a strong ramp across the wavelength range of interest, while the albedo and phase function dominate the overall shape of the spectrum (its peak near 2–3 μm); for this reason, we focus on Q_{ext} to explain the improvement in the fit of the 2.87 μm feature in the DDA models.

We next note that Q_{ext} can be related to the phase shift of a wave passing through a particle. These absorbing particles with large x fall under anomalous diffraction theory, and in the range where n_r is close to unity (which also means a small relative phase change $\rho = 2x|n_r - 1| \ll 1$), the extinction efficiency Q_{ext} is a monotonically increasing function of ρ (Fig. 15; see Van de Hulst, 1957,

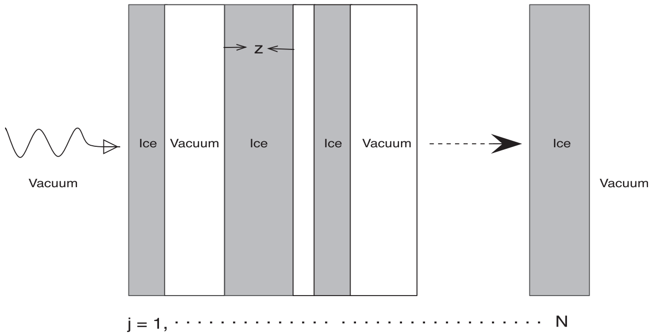

Fig. 16. Multilayer toy model consists of randomly placed, alternating layers of ice and vacuum with complex refractive index m_j and thickness z_j which can vary randomly between 0 and 6 μm. The total length of the multilayer is kept constant at a value representative of the mean diameter of our aggregate size distribution (about 30 μm). We generate many realizations of such multilayers, all having the same average density and total thickness.

Chapter 11.23). The parameter ρ is a nominal phase difference between a wave traversing a dielectric medium without interfaces and one that has gone the same distance undisturbed. Since Q_{ext} dominates the Christiansen feature (Fig. 14), how fast Q_{ext} increases away from the linear region near $n_r = 1$ or $|m-1| \approx 0$ where it is a minimum, as wavelength varies, dictates the depth and width of the band. Particles with larger phase shifts have higher Q_{ext} and can remove energy from the incident EM wave more efficiently.

While ρ is a good general way to parameterize the extinction efficiency (Q_{ext}), the real phase change through a complicated particle – an aggregate or multilayer – has extra terms related to the phase changes arising from reflection and transmission at the various interfaces. An aggregate with overlapping monomers has many optical interfaces and various pathways of varying lengths for a traveling electromagnetic (EM) wave. We model an aggregate by a dielectric multilayer of ice–vacuum layers with varying thicknesses. Analytical solutions can be written for the complex transmission and reflection coefficients of such multilayers (Born and Wolf, 1999, Chapters 1 and 14) which include the net phase change of the wave and explicitly identify these interface terms. We vary the thickness and distances between the layers randomly, keeping the aggregate porosity constant by keeping the ratio of the ice to air layers the same for the various configurations. We then average the phase change through many realizations of such multilayers to capture the general behavior of the phase change through an aggregate. A Mie–EMT particle is modeled by a uniform single layer with the EMT optical constants for the desired porosity. Given that the parameter ρ, or relative phase, is a way to characterize the behavior of Q_{ext} for a particle, we estimate the scattering difference between an aggregate and a uniform particle by calculating the phase change of an EM wave traveling through an ice–air multilayer *relative* to a wave passing through a uniform layer of the same total mass.

We calculate the transmission through a multilayer (see Fig. 16) by using the characteristic matrix M for a single layer of thickness z and complex refractive index m at normal incidence (Born and Wolf, 1999). The characteristic matrix of the multilayer M^T is found by multiplying the single layer characteristic matrices (see Eqs. (7) and (8)). The final transmission coefficient t is obtained by calculating the matrix elements of M^T (Eq. (8)). The transmission coefficient is the ratio of the transmitted electric field to the incident electric field; it can be written in terms of the phase shift ϕ of the transmitted field after the multilayer $t = |t|e^{i\phi}$.

$$M(z_j, m_j) = \begin{vmatrix} M^j_{11} & M^j_{12} \\ M^j_{21} & M^j_{22} \end{vmatrix}; \quad \begin{aligned} M^j_{11} &= M^j_{22} = cos(km_jz_j) \\ M^j_{12} &= -\tfrac{i}{m_j} sin(km_jz_j), \\ M^j_{21} &= -i\,m_j\, sin(km_jz_j) \end{aligned} \tag{10}$$

$$M^T = \prod_{j=1}^{N} M(z_j, m_j); \quad t = \frac{2}{(M^T_{11} + M^T_{12}) + (M^T_{21} + M^T_{22})} \tag{11}$$

The difference in phase change between traversal of a multilayer and a single layer is plotted in Fig. 17. The most obvious feature in the phase change of Fig. 17 (at 3.1 μm) is not seen in the data, for reasons explained in the caption. Instead, we focus on the more subtle and more interesting behavior near 2.87 μm. Note that the phase difference goes through zero where $n_r = 1$, as

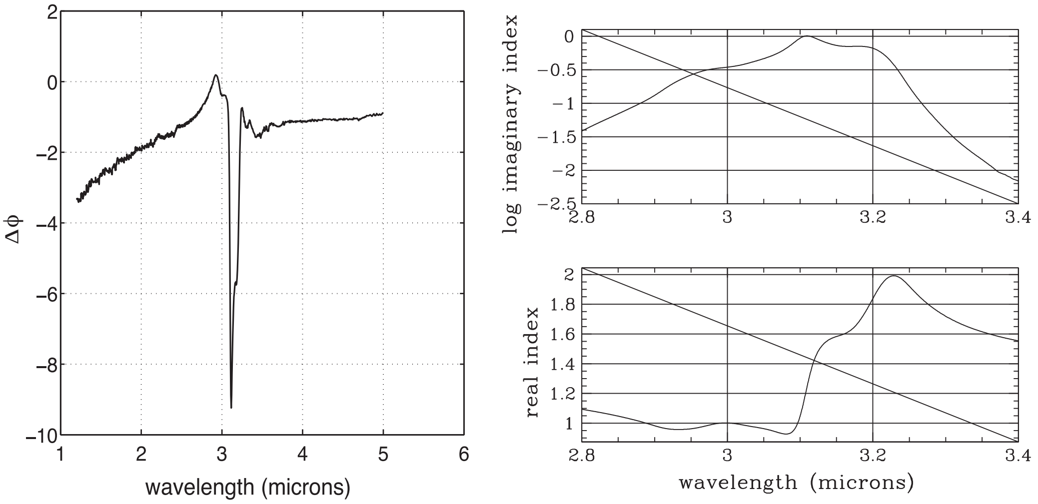

Fig. 17. (Left) Transmitted phase difference $\Delta\phi$ (radians) between an ice–air multilayer and single ice layer with 30% porosity and 30 μm thickness versus λ (μm). There are three main features in this plot: (1) the phase difference sharp rise and fall about 2.87 μm is where the transmitted EM wave accumulates a larger phase change after going through the multilayer interfaces compared to a single layer (see Section 3.5); (2) the asymmetric slope of the phase change below and above ~3 μm affects the size distribution used in the DDA model (represented by a multilayer) compared to that used in the Mie–EMT model (represented by a single layer) (see Section 3.5); and finally (3) another large accumulation of phase change is at 3.1 μm where the interfaces of a multilayer play a large role due to the large imaginary index at this wavelength (see right panels for optical constants). However, we do not see this feature in the observed spectrum because the particles are absorbing with a large imaginary index and Q_{ext} never gets small. That is, the energy transmitted through the particle is negligible and its effects are insensitive to the details of its phase shift, as opposed to the phase-shift-sensitive behavior at the Christiansen frequency where the energy transmitted is significant.

expected from $\rho = 2x|m-1|$ (if $n_i \ll 1$). The ice–vacuum multilayer quickly obtains a greater phase shift, moving away from the 2.87 μm Christiansen frequency, relative to a single layer of the same porosity. This more rapidly changing phase difference indicates that Q_{ext} is changing faster for a multilayer, or moving away from $Q_{ext} = 0$ (at $n_r = 1$) faster, than for a single layer. The reason is that the final emergent wave in the multilayer problem has contributions that represent no reflections, two reflections, four reflections, etc. (from here on referred to as the "interface terms"). The multi reflection cases have larger paths over which to accumulate phase shift. The phase shifts may be larger than 2π, but as you vary the spacings randomly, and average the results, the net effect of adding the multi reflection components with random phase shifts is that the net change in phase will be larger for a multilayer than for a solid slab with the same mass/area. At the Christiansen frequency the reflection coefficients get very small; here, the multi reflection contribution is negligible so the multislab and single slab cases give the same phase shift. The aggregate also has this "feature" of having multi reflection paths in addition to the straight through paths. This will have little effect *at* the Christiansen frequency, but will lead to larger phase shifts close to, and on either side of, the Christiansen frequency. We can conclude that a multilayer representing an aggregate is a better scatterer, and able to diffract more energy at smaller n_r, which is why aggregates have a deeper band.

Moreover, the relative phase change also has a greater slope at wavelengths shorter than ~3 μm than at longer wavelengths. This effect also explains why our DDA spectra require different particle size distributions than our Mie–EMT models – the DDA models call for a distribution with fewer small particles (starting around 13–30 μm) than the EMT models. Since the smaller aggregates are those which are diffracting into the instrument at the shorter wavelengths, at these high phase angles, and aggregates are better scatterers than uniform particles, fewer of the small aggregates can be allowed for consistency with the data. However at the large wavelength end the scattering properties are similar for aggregates and uniform particles, as we can see in the constant phase difference, because these longer wavelengths blur the interfaces between wavelength and size monomers, causing the "interface" terms to become less important. Thus, for $\lambda > 3$ μm, the DDA models provide a similar fit to the EMT models with the same size distribution (10–30 μm).

4. Conclusion

Our Mie–EMT modeling has restricted the particle size distribution to a limited range between 10 and 30 μm. Further tests can be done to investigate the exact nature of the rolloff at the limits of the size distribution, but for our purposes an estimate of the size range is enough to get the general profile of the spectra. Our modeling has also constrained the particle composition using the wavelength of the central dip in the spectrum, which is very sensitive to composition at high phase angles. We found that crystalline ice best captures the position of the central dip, as opposed to amorphous ice which shows a dip at a shorter wavelength than observed. Diffraction dominates the overall spectral shape, and the only spectral feature that shows up is at the Christiansen frequency where the real part of the refractive index goes through unity and the imaginary part remains very small, so the particles' optical activity is drastically reduced. We further explored the possibility of aggregates by using the DDA approach and found that aggregates with a size distribution similar to the Mie–EMT models provide a better fit for the depth and width of the central band. The two modeling approaches imply slightly different size distributions, which can be explained by a simple dielectric multilayer toy model. Aggregates are more effective scatterers than uniform particles, and hence have a deeper 2.87 μm band and asymmetric spectral shape. This is because of the many surface-interface reflections which become more important at shorter wavelengths and higher refractive indices. Another implication is that no other material besides water ice can be present with a significant fractional abundance, because no other common material has $n_r = 1$ at 2.87 μm. This confirms that crystalline water ice must be the dominant component in the F ring particles.

Acknowledgments

We are very grateful to Kathy Rages for providing her Mie scattering code and for assistance fixing problems it developed with the unusual set of refractive indices we were using. We have profited greatly from generous allocations of cpu time on the NASA High-End Computing (HEC) machines at Ames. In addition to raw cycles, expert consultants have provided invaluable help in parallelization and optimization. We'd like to thank Terry Nelson, Piyush Mehrotra, and especially Art Lazanoff for help getting the optimizing done, Denis Richard for his help testing the code, Rachel Mastrapa for providing data in advance of publication and several helpful conversations, observation designers on the VIMS team, Essam Marouf and Frank Bridges for insightful conversations. The research was partially supported by the Cassini project and partially by a grant to JNC from NASA's Planetary Geology and Geophysics program.

References

Arnott, W.P., Dong, Y.Y., Hallett, J., 1995. Extinction efficiency in the infrared (218 μm) of laboratory ice clouds: Observations of scattering minima in the Christiansen bands of ice. Appl. Opt. 34 (3), 541–551.

Bertie, J.E., Jacobs, S.M., 1977. Far-infrared absorption by ices Ih and Ic at 4.3 K and the powder diffraction pattern of ice Ic. J. Chem. Phys. 67, 2445–2448.

Bertie, J.E., 1969. Absorptivity of Ice I in the range 4000–30 cm^{-1}. J. Chem. Phys. 50, 4501.

Barbara, J.M., Esposito, L.W., 2002. Moonlet collisions and the effects of tidally modified accretion in Saturn's F ring. Icarus 160 (1), 161–171.

Bosh, A.S., Olkin, C.B., French, R.G., Nicholson, P.D., 2002. Saturn's F ring: Kinematics and particle sizes from stellar occultation studies. Icarus 157 (1), 57–75.

Bosh, A.S., Rivkin, A.S., Percival, J.W., Taylord, M., van Citterse, G.W., 1997. Saturn ring-plane crossing, May 1995: Pole precession and ring thickness. Icarus 129 (2), 555–561.

Bohren, C.F., Huffman, D.R., 1983. Absorption and Scattering of Light by Small Particles. Wiley, New York.

Born, M., Wolf, E., 1999. Principles of Optics, seventh ed. Cambridge University Press.

Brown, R.H., Baines, K.H., Bellucci, G., Bibring, J.P., Buratti, B.J., Capaccioni, F., et al., 2004. The Cassini Visual and Infrared Mapping Spectrometer (VIMS) investigation. Space Sci. Rev. 115, 111–168.

Chandrasekhar, S., 1960. Radiative Transfer. Dover, New York.

Charnoz, S., Porco, C.C., Deu, E., Brahic, A., Spitale, J.N., Bacques, G., et al., 2005. Cassini discovers a kinematic spiral ring around Saturn. Science 310 (5752), 1300–1304.

Conel, J.E., 1969. Infrared emissivities of silicates: Experimental results and a cloudy atmosphere model of spectral emission from condensed particulate mediums. J. Geophys. Res. 74, 1614–1634.

Cuzzi, J.N., 1985. Rings of Uranus – Not so thick, not so black. Icarus 63 (2), 312–316.

Cuzzi, J.N., Burns, J.A., 1988. Charged particle depletion surrounding Saturn's F ring: Evidence for a moonlet belt? Icarus 74 (2), 284–324.

Cuzzi, J., Clark, R., Filacchione, G., French, R., Johnson, R., Marouf, E., et al., 2009. Ring particle composition and size distribution. In: Dougherty, M., Brown, R., Waite, H. (Eds.), The Saturn System after Cassini-Huygens. Springer.

Cuzzi, J.N., Estrada, P.R., 1998. Compositional evolution of Saturn's rings due to meteoroid bombardment. Icarus 132 (1), 1–35.

Draine, B.T., Allaf-Akbari, K., 2006. X-ray scattering by nonspherical grains. I. Oblate spheroids. Astrophys. J. 652, 1318–1330.

Draine, B.T., Flatau, P.J., 1994. Discrete dipole approximation for scattering calculations. J. Opt. Soc. Am. 11, 1491–1499.

Esposito, L.W., Cuzzi, J.N., Holberg, J.B., Marouf, E.A., Tyler, G.L., Porco, C.C., 1984. Saturn's Rings – Structure, Dynamics, and Particle Properties. Saturn University of Arizona Press, pp. 463–545.

Hansen, J.E., Travis, L.D., 1975. Light scattering in planetary atmospheres. Space Sci. Rev. 16, 527–610.

Hedman, M.M., Nicholson, P.D., Showalter, M.R., Brown, R.H., Buratti, B.J., Clark, R.N., Baines, K., Sotin, C., 2011. The Christiansen effect in Saturn's narrow dusty rings

and the spectral identification of clumps in the F ring. Icarus, accepted for publication.
Hedman, M.M., Nicholson, P.D., Showalter, M.R., Brown, R.H., Buratti, B.J., Clark, R.N., 2009. Spectral observations of the Enceladus plume with Cassini–VIMS. Astrophys. J. 693, 1749–1762.
Hornig, D.F., White, H.F., Reding, F.P., 1958. The infrared spectra of crystallline H_2O, D_2O and HDO. Spectrochim. Acta 12, 338–349.
Hudgins, D.M., Sandford, S.A., Allamandola, L.J., Tielens, A.G., 1993. Mid- and far-infrared spectroscopy of ices – Optical constants and integrated absorbances. Astrophys. J. Suppl. Ser. 86 (2), 713–870.
Lane, A.L., Hord, C.W., West, R.A., Esposito, L.W., Coffeen, D.L., Sato, M., et al., 1982. Photopolarimetry from Voyager 2; Preliminary results on Saturn, Titan, and the rings. Science 215 (4532), 537–543.
Leger, A., Gauthier, S., Defourneau, D., Rouan, D., 1983. Properties of amorphous H_2O ice and origin of the 3.1-micron absorption. Astron. Astrophys. 117 (1), 164–169.
Mastrapa, R.M., Sandford, S.A., Roush, T.L., Cruikshank, D.P., Dalle Ore, C.M., 2009. Optical constants of amorphous and crystalline H_2O–ice: 2.5–22 μm (4000–455 cm^{-1}). Astrophys. J. 701, 1347–1356.
Mastrapa, R.M., Bernstein, M.P., Sandford, S.A., Roush, T.L., Cruikshank, D.P., Dalle Ore, C.M., 2008. Optical constants of amorphous and crystalline H_2O–ice in the near infrared from 1.1 to 2.6 m. Icarus 197 (1), 307–320.
McCord, T.B., Coradini, A., Hibbitts, C.A., Capaccioni, F., Hansen, G.B., Filacchione, G., Clark, R.N., Cerroni, P., Brown, R.H., Baines, K.H., Bellucci, G., Bibring, J.P., Buratti, B.J., Bussoletti, E., Combes, M., Cruikshank, D.P., Drossart, P., Formisano, V., Jaumann, R., Langevin, Y., Matson, D.L., Nelson, R.M., Nicholson, P.D., Sicardy, B., Sotin, C., 2004. Cassini VIMS observations of the Galilean satellites including the VIMS calibration procedure. Icarus 172 (1), 104–126.
Murray, C.D., Beurle, K., Cooper, N.J., Evans, M.W., Williams, G.A., Charnoz, S., 2008. The determination of the structure of Saturn's F ring by nearby moonlets. Nature 453, 739–744.
Murray, C.D., Gordon, M.K., Giuliatti Winter, S.M., 1997. Unraveling the strands of Saturn's F ring. Icarus 129 (2), 304–316.
Mustard, J.F., Hays, J.E., 1997. Effects of hyperfine particles on reflectance spectra from 0.3 to 25 microns. Icarus 125, 145–163.
Nicholson, P.D., French, R.G., Tollestrup, E., Cuzzi, J.N., Harrington, J., Matthews, K., Perkovi, O., Stoverg, R.J., 2000. Saturn's rings I: Optical depth profiles from the 28 Sgr occultation. Icarus 145 (2), 474–501.
Nicholson, P.D., Hedman, M.M., Clark, R.N., Showalter, M.R., Cruikshank, D.P., Cuzzi, J.N., Filacchione, G., Capaccioni, F., Cerroni, P., Hansen, G.B., Sicardy, B., Drossart, P., Brown, R.H., Buratti, B.J., Baines, K.H., Coradini, A., 2008. A close look at Saturn's rings with Cassini VIMS. Icarus 193 (1), 182–212.
Nicholson, P.D., Hedman, M.M., Wallis, B.D., 2007. Cassini–VIMS team Cassini–VIMS observations of stellar occultations by Saturn's rings. AAS/DDA Meeting 38, 12.05.
Ockman, N., 1958. The infra-red and Raman spectra of Ice. Adv. Phys. 7, 199–220.
Pollack, J.B., Cuzzi, J.N., 1980. Scattering by nonspherical particles of size comparable to a wavelength: A new semi-empirical theory and its application to tropospheric aerosols. J. Atmos. Sci. 37 (4), 868–881.
Poulet, F., Cruikshank, D.P., Cuzzi, J.N., Roush, T.L., French, R.G., 2003. Compositions of Saturn's rings A, B, and C from high resolution near-infrared spectroscopic observations. Astron. Astrophys. 412, 305–316.
Purcell, E.M., Pennypacker, C., 1973. Scattering and absorption of light by nonspherical dielectric grains. Astrophys. J. 186, 705–714.
Scargle, J., Cuzzi, J.N., Dobrovolskis, A., Dones, L., Hogan, R., Levit, C., et al., 1993. Dynamical evolution of Saturn's rings. AAS Meeting 25, 26.04.
Shen, Y., Draine, B.T., Johnson, E.T., 2008. Modeling porous dust grains with ballistic aggregates. I: Geometry and optical properties. Astrophys. J. 689, 260–275.
Showalter, M.R., Cuzzi, J.N., Larson, S.M., 1991. Structure and particle properties of Saturn's E ring. Icarus 94 (2), 451–473.
Showalter, M.R., French, R., Sfair, R., Argelles, C., Pajuelo, M., Becerra, P., et al., 2009. The brightening of Saturn's F ring. 2009 DPS Meeting.
Showalter, M.R., Burns, J.A., 1982. A numerical study of Saturn's F-ring. Icarus 52 (3), 526–544.
Showalter, M.R., Pollack, J.B., Ockert, M.E., Doyle, L.R., Dalton, J.B., 1992. A photometric study of Saturn's ring. Icarus 100 (2), 394–411.
Smith, B.A., Soderblom, L., Beebe, R., Boyce, J., Briggs, G., Bunker, A., et al., 1981. Encounter with Saturn: Voyager 1 imaging science results. Science 212 (4491), 163–191.
Smith, B.A., Soderblom, L., Batson, R., Bridges, P., Inge, J., Masursky, H., et al., 1982. A new look at the Saturn system: The Voyager 2 images. Science 215 (4532), 504–537.
Throop, H.B., Esposito, L.W., 1998. G ring particle sizes derived from ring plane crossing observations. Icarus 131 (1), 152–166.
Tyler, G.L., Marouf, E.A., Simpson, R.A., Zebker, H.A., Eshleman, V.R., 1983. The microwave opacity of Saturn's rings at wavelengths of 3.6 and 13 cm from Voyager 1 radio occultation. Icarus 54 (2), 160–188.
Van de Hulst, H.C., 1957. Light Scattering by Small Particles. Wiley, New York.
Winter, O.C., Mouro, D.C., Giuliatti Winter, S.M., Spahn, F., da Cruz, C., 2007. Moonlets wandering on a leash-ring. Mon. Not. R. Astron. Soc. 380 (1), L54–L57.